Low-lying excited states in crystalline perylene

Tonatiuh Rangel[a,b,1], Andre Rinn[c,1], Sahar Sharifzadeh[d,e], Felipe H. da Jornada[b,f], André Pick[c], Steven G. Louie[b,f], Gregor Witte[c], Leeor Kronik[g,2], Jeffrey B. Neaton[a,b,h,2], and Sangam Chatterjee[c,i,2]

[a]Molecular Foundry, Lawrence Berkeley National Laboratory, Berkeley, CA 94720; [b]Department of Physics, University of California, Berkeley, CA 94720; [c]Faculty of Physics and Materials Sciences Center, Philipps-Universität Marburg, D-35032 Marburg, Germany; [d]Department of Electrical and Computer Engineering, Boston University, Boston, MA 02215; [e]Materials Science and Engineering Division, Boston University, Boston, MA 02215; [f]Materials Sciences Division, Lawrence Berkeley National Laboratory, Berkeley, CA 94720; [g]Department of Materials and Interfaces, Weizmann Institute of Science, Rehovoth, 76100, Israel; [h]Kavil Energy NanoSciences Institute at Berkeley, Berkeley, CA 94720; and [i]Institute of Experimental Physics I, Justus Liebig University Giessen, D-35392 Giessen, Germany

Edited by Peter J. Rossky, Rice University, Houston, TX, and approved November 27, 2017 (received for review July 2, 2017)

Organic materials are promising candidates for advanced optoelectronics and are used in light-emitting diodes and photovoltaics. However, the underlying mechanisms allowing the formation of excited states responsible for device functionality, such as exciton generation and charge separation, are insufficiently understood. This is partly due to the wide range of existing crystalline polymorphs depending on sample preparation conditions. Here, we determine the linear optical response of thin-film single-crystal perylene samples of distinct polymorphs in transmission and reflection geometries. The sample quality allows for unprecedented high-resolution spectroscopy, which offers an ideal opportunity for judicious comparison between theory and experiment. Excellent agreement with first-principles calculations for the absorption based on the GW plus Bethe–Salpeter equation (GW-BSE) approach of many-body perturbation theory (MBPT) is obtained, from which a clear picture of the low-lying excitations in perylene emerges, including evidence of an exciton–polariton stopband, as well as an assessment of the commonly used Tamm–Dancoff approximation to the GW-BSE approach. Our findings on this well-controlled system can guide understanding and development of advanced molecular solids and functionalization for applications.

molecular crystals | many-body perturbation theory | excited states | spectroscopy

Organic semiconductors promise to play a major role in future technologies (1, 2) and are already present in advanced solar cells and light-emitting diodes. Such materials can feature strong optical absorption and mechanical flexibility; and they are readily manufactured as thin films, for example, by printing techniques on various substrates. At the same time, organic semiconductors possess complex photophysical properties. Molecular solids, a subset of organic semiconductors, consist of covalently bound molecular units linked via weak (typically van der Waals) interactions. The optical spectra of molecular crystals based on polyaromatic conjugated hydrocarbons feature strongly bound excitons, with binding energies of several hundreds of millielectronvolts, as well as significant singlet–triplet exchange splittings on the same energy scale. Both are comparable to intermolecular binding energies occurring in these van der Waals-bound solids (3–6). Furthermore, the large singlet–triplet splittings can facilitate singlet exciton fission, a carrier multiplication mechanism which enables quantum efficiencies beyond the Shockley–Queisser limit (7). The common presence of static disorder in polycrystalline molecular solids leads to significant challenges in obtaining a comprehensive understanding of optical excitation processes, mandating the need for comprehensive studies on very highly ordered, single-crystal model systems (1).

Perylene is a well-studied prototypical material as it is the parent molecule for a vast class of dyes. Prior studies of crystals based on perylene and its derivatives have revealed strong light–matter interactions and low-lying exciton bands exhibiting significant anisotropic absorption, (8–14) similar to the acenes. Microscopically, this can be traced back to the near-direct gap nature of the electronic band structure and strong overlap of the quasi-delocalized π and π^* frontier molecular orbitals. Typically, spectroscopic studies are performed with large-scale crystalline samples, where the large oscillator strengths (and hence strong absorption) of molecular solids prohibit the use of transmission geometry due to limitations in dynamic range. Therefore, experiments are often performed in reflection geometry and are analyzed by using the Kramers–Kronig transformation (15–17), a relation only rigorously valid if the entire spectrum is considered.

Prior transmission studies of perylene and coronene have not been able to distinguish fully between the multiple exciton lines due to sample quality (18). Recent advances in crystal growth, however, facilitated a polymorph-selective preparation of thin perylene single crystallites with thicknesses of few hundred nanometers and lateral extensions of 50 μm (19). The exceptional quality of their surfaces, with negligible roughness, and their low sample thickness allow for a comparison between high-resolution polarization-resolved linear absorption spectroscopy in transmission, similar reflection measurements, and state-of-the-art theory.

Theoretical studies of excited-state properties have been performed for acenes (20–32), such as pentacene, and related

Significance

Molecular solids are an important class of highly tunable, chemically diverse, cheap-to-process materials with promise for next-generation organic optoelectronics. Bound largely by noncovalent interactions, these materials harbor unique charge carrier generation and transport phenomena distinct from conventional semiconductors, an understanding of which requires a detailed description of the excited-state properties of molecular solids. Recent advances in synthetic techniques, ab initio theory, and spectroscopic measurements have enabled such a description, and here we perform quantitative theoretical calculations and high-resolution measurements on a high-quality single-crystal thin film of perylene, an exemplar molecular solid. We obtain excellent agreement between theory and experiment, and a clear picture of the low-lying excitations in perylene responsible for its distinctive optical properties.

Author contributions: S.G.L., G.W., L.K., J.B.N., and S.C. designed research; T.R., A.R., S.S., F.H.J., A.P., S.G.L., G.W., L.K., J.B.N., and S.C. performed research; T.R., A.R., S.S., F.H.J., A.P., S.G.L., G.W., L.K., J.B.N., and S.C. analyzed data; and T.R., S.S., F.H.J., S.G.L., L.K., J.B.N., and S.C. wrote the paper.

The authors declare no conflict of interest.

This article is a PNAS Direct Submission.

[1]T.R. and A.R. contributed equally to this work.

[2]To whom correspondence may be addressed. Email: leeor.kronik@weizmann.ac.il, jbneaton@berkeley.edu, or sangam.chatterjee@physik.uni-giessen.de.

This article contains supporting information online at www.pnas.org/lookup/suppl/doi:10.1073/pnas.1711126115/-/DCSupplemental.

functionalized organic crystals (33), using many-body perturbation theory within the GW approximation (34–36) and the Bethe–Salpeter equation (BSE) approach (37, 38), based on a density functional theory (DFT) starting point. These calculations have yielded excellent agreement with experiment and provided insights into excited-state properties of acene crystals. Prior theoretical work on perylene has been performed using DFT or time-dependent DFT. For perylene monomers in solution, it was found that substituents can controllably alter stability, orbital level energetics, charge transport, and optical absorption (39), suggesting routes for impacting performance in the condensed phase. In addition, calculations of perylene in the solid state have predicted accurate lattice parameters by accounting for van der Waals interactions and have predicted a fundamental indirect bandgap (40). However, thus far we are unaware of first-principles calculations for optical absorption in solid perylene. As time-dependent DFT using standard approximations for the exchange-correlation functional fails to capture excitonic effects (see, e.g., refs. 6 and 25), and given the high spectral resolution required here, we use GW-BSE in what follows, the gold standard approach for accurate computation of optical excitations of solids.

Here, we compare high-resolution linear absorption spectroscopy on high-quality perylene single crystals to first-principles GW-BSE calculations, finding excellent agreement for both perylene polymorphs. We explain the origin and nature of low-lying neutral excitations, identify higher-order collective effects—notably an exciton–polariton stopband—and examine the possible limitations of the well-established Tamm–Dancoff approximation (TDA) in solving the BSE for the present system.

Methods

Perylene crystals are prepared by liquid-mediated growth onto thin films of silicone oil spin-coated on a quartz substrate. This yields platelet-shaped (100)-oriented single crystals with molecularly flat surfaces, thicknesses below 300 nm, and lateral extensions of 20–50 μm. Tuning of the growth parameters (substrate temperature and molecular flux) enables further a polymorph-selective growth of individual perylene crystals of both phases. As demonstrated in previous work (19), the respective phases as well as the azimuthal directions can be easily identified due to the characteristic crystalline shapes (so-called *tracht*; Fig. 1). Additional crystals were prepared by repeated resublimation of perylene powder onto oxidized Si wafers as described in ref. 19, yielding thicker samples which are used for the reflection measurements. All optical measurements are performed using a microscope setup with a spatial resolution below 5 μm, featuring all-reflective optics to avoid chromatic aberrations and ensure a high throughput of UV light wherever possible. The spectra are obtained using a water-cooled deuterium arc lamp as a light source and a grating spectrometer equipped with a scientific-grade charge-coupled device for detection. A wire grid-polarizer is used to achieve a polarization contrast better than 100:1. Reflection data are obtained in confocal microscopy geometry, again featuring all-reflective optics. A conventional tungsten–halogen lamp is used as the light source for the reflection measurement. Experiments are performed at a sample-holder temperature of 5 K in a liquid helium flow cryostat, yielding a narrowing of the spectral line width compared with room temperature data. Time-resolved photoluminescence is measured using a streak camera setup with similar optical components as in the absorption measurements for high spatial resolution and to prevent chromatic aberrations. The samples are excited with a pulsed, frequency-doubled femtosecond Ti:sapphire laser at 400 nm with 20 μW of average power. Spectral resolution is achieved with a grating spectrometer. The S20 photocathode in the streak camera enables temporal resolution of <2 ps. The signal is measured around the respective PL maxima of the samples, integrated over a spectral window of 20-nm width. Absorption spectroscopy is performed in the vapor phase using a xenon-arc lamp as a light source. Perylene powder is placed in a heated chamber specifically designed for this purpose. The chamber is evacuated to below 10^{-6} mbar to prevent oxidation and absorption from residual gas. The chamber is then heated to 470 K to evaporate the perylene and prevent resublimation on the walls and windows. The transmission is compared with reference data taken on a second, equally constructed yet empty cell. The same detection setup with grating spectrometer and camera is used to obtain the spectra as in the measurement on the solid samples.

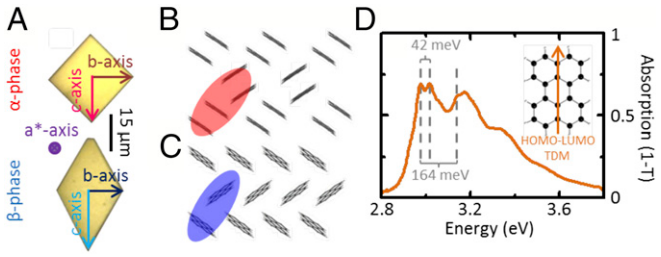

Fig. 1. Perylene single-crystal samples and structure: Microscopy images of (100)-oriented perylene single crystals in the α-phase (*Top*) and the β-phase (*Bottom*) (*A*), identifiable by their respective characteristic nearly rectangular and rhombic shapes. The crystalline axes given by the arrows are universal for *A*–*C*; the depicted crystals are correctly aligned to the shown molecular packing motives. Molecular orientation in α-phase perylene is found in *B*. The unit cell contains four molecules (red oval), where pairs of parallelly oriented molecules form a dimeric herringbone motif. The corresponding picture for the β-phase is presented in *C*. Its unit cell comprises two molecules forming a standard herringbone stacking pattern (blue oval). The light field is incident along the depicted $\vec{a}^*$ axis. The linear absorption spectrum of perylene in the vapor phase is displayed in *D*. The HOMO–LUMO transition is assigned at 2.98 eV. Linear combinations of two vibrons with energies of 42 and 164 meV lead to a series of vibronic progressions. The *Inset* shows the perylene molecule and the alignment of the transition dipole moment (TDM) for the known HOMO–LUMO transition.

Quasiparticle excitation energies are computed within the GW approximation, which accounts for electron–electron correlations and screening explicitly by expanding the electronic self-energy Σ to lowest order in W, $\Sigma = iGW$ (34, 35). Here, G is the one-electron Green's function of the system, $W = \varepsilon^{-1}v$ is the dynamically screened coulomb potential, v is the bare coulomb potential, and ε is the wavevector and frequency-dependent dielectric matrix. The GW quasiparticle energies are computed perturbatively starting from Kohn–Sham DFT orbitals and eigenvalues (34–36). Subsequently, the optical response is calculated by solving the BSE, which in its full form (i.e., beyond the TDA) has the block-matrix structure:

$$\begin{pmatrix} A & B \\ -B^* & -A^* \end{pmatrix} \begin{pmatrix} X^S \\ Y^S \end{pmatrix} = \Omega^S \begin{pmatrix} X^S \\ Y^S \end{pmatrix}, \quad [1]$$

where Ω^S are the neutral excitation energies, A and B are coupling matrices constructed from the GW quasiparticle energies and Kohn–Sham orbitals, and (X^S, Y^S) are eigenstates from which the oscillator strength and the nature of the optical transition can be computed (37, 38). Importantly, A and B incorporate direct screened electron–hole interactions, as well as exact exchange. In the TDA, the B term that couples excitations to deexcitations is neglected to gain computational efficiency, and hence the BSE decouples into two equations. Here, we perform calculations both with and without the TDA (41).

In this work, our DFT calculations are performed using a plane-wave basis and norm-conserving pseudopotentials with the ABINIT code (42). We fix the perylene lattice parameters to those measured at low temperatures (43) and relax the internal coordinates using the Perdew–Burke–Ernzerhof functional (44). We note that the lattice parameters we use were measured at 150–200 K (43), temperatures higher than that of the spectroscopy measurements in this work (5 K); this is acceptable, as our own temperature-dependent linear absorption spectra (*Supporting Information*) reveal no spectral shifts in the range from 5 to 290 K. Our GW calculations are performed using the BerkeleyGW code (45). As discussed below, we use sufficient plane-wave cutoffs and unoccupied states to converge quasiparticle gaps to ∼0.1 eV, following previous work (21–23). The frequency dependence of the dielectric function is obtained using the generalized plasmon-pole model of Hybertsen and Louie (36). We use an energy cutoff of 10 Ry to truncate the plane-wave sums used for the calculation of the polarizability. We use a grid of 3 × 3 × 3 and 3 × 5 × 3 k-points for the GW calculations of the α- and β-phases of perylene, respectively. We sum over a number of unoccupied bands equivalent to an energy range of 30 eV above the lowest unoccupied state and solve the BSE Hamiltonian with 10 valence bands and 10 conduction bands at each k-point. We use two k-point meshes: a coarse grid corresponding to that used in the GW step with which we calculate the BSE kernel; and a fine grid of 6 × 6 × 5 and 6 × 10 × 6 for the α- and β-phases, respectively, to calculate the optical absorption spectra. This set of parameters results in a convergence in the energy position of the calculated low-lying excitations within 10 meV. We

solve the BSE Hamiltonian using a generalized non-Hermitian matrix solver, as discussed in ref. 41.

Results and Discussion

Perylene exhibits two monoclinic phases, both of which possess $P2_1/c$-symmetry: the α-polymorph contains four molecules per unit cell arranged in a sandwich-herringbone motif, while the β-polymorph has two molecules within the unit cell arranged in a monomeric herringbone motif (43). Both polymorphs are easily distinguishable based on their appearance: the (100)-oriented α- and β-phase crystals reveal an almost quadratic or rhombic base area, respectively (19), as depicted in Fig. 1*A*. The related molecular packing, seen from a top view (i.e., along $\vec{a}^*$) onto the $(\vec{b},\vec{c})$-plane of both phases, is depicted in Fig. 1 *B* and *C*. The fundamental (lowest energy) singlet transition is observed at 2.98 eV in the gas phase (Fig. 1*D*), with pronounced excited-state vibronic replica found for $h\nu_1 = 42$ meV, $h\nu_2 = 164$ meV, and their linear combinations, respectively (46–48). The transition dipole moment (TDM) of this lowest singlet excitation [S_1, highest occupied molecular orbital (HOMO)–lowest unoccupied molecular orbital (LUMO) transition (49)] is oriented along the long molecular axis (50), as shown in the *Inset* of Fig. 1*D*. The polarization-dependent linear optical response, deduced from transmission and reflection measurements, provides direct access to the excitonic optical excitations of perylene, as well as the oscillator strengths of these excitations and their spatial orientation. In the present study, only those excitations with TDM components oriented within the $(\vec{b},\vec{c})$-plane are addressed in transmission geometry, as the light is incident along the $\vec{a}^*$ axis. Since the perylene molecules stand nearly upright within the (100)-plane [96.77° and 100.92° for the α- and β-phases, respectively (43)], the TDM of S_1 exhibits only weak coupling with the electric-field vector $\vec{E}$ of the incident light polarized perpendicular to $\vec{a}^*$. Nevertheless, the polarization-resolved spectra clearly reveal a distinct azimuthal dependence of the excitonic resonances.

Measured transmission (T) spectra of α- and β-perylene crystallites are presented as (1-T) plots in Fig. 2 *A* and *B*, respectively. The curves in dark (light) colors denote measurements with light polarized along the $\vec{b}$ axis ($\vec{c}$ axis). Several resonances are observed and assigned to exciton-like transitions and their vibronic replica (51). The lowest-energy peaks appear around 2.6 eV, about 0.4 eV below the first excitation in the gas phase. They are attributed to the fundamental bright exciton transition, which defines the optical band gap and exhibits a Davydov splitting of 33 meV for the α-phase and 30 meV for the β-phase. The higher-energy Davydov component of both polymorphs is accessible with light polarized along the $\vec{c}$ axis and exhibits a significantly lower oscillator strength than that accessible with light polarized along the $\vec{b}$ axis. Compared with the β-phase, the α-phase exhibits more pronounced vibronic replicas, attributed to the more complex packing motif with four molecules in the unit cell yielding a larger vibronic density of states and possibly different coupling strengths. The pronounced features at 2.68 and 2.81 eV, observed for α-phase crystals under polarization along the $\vec{b}$ axis, are identified as vibronic replicas by comparison with Raman spectra reported in the literature, overlapping with an exciton mode in the latter case (51). Those transitions are marked by a ν in Fig. 2.

Prior work has discussed the nature of peaks in the linear absorption spectrum of perylene in terms of an extension of Kasha's rules, intuition developed for rationalizing changes in spectroscopic features, relative to the gas phase, that depend on the alignment of and interactions between chromophore transition dipoles in dimers and more complex aggregates (52, 53). Within this framework, our measurements on both perylene phases show signatures

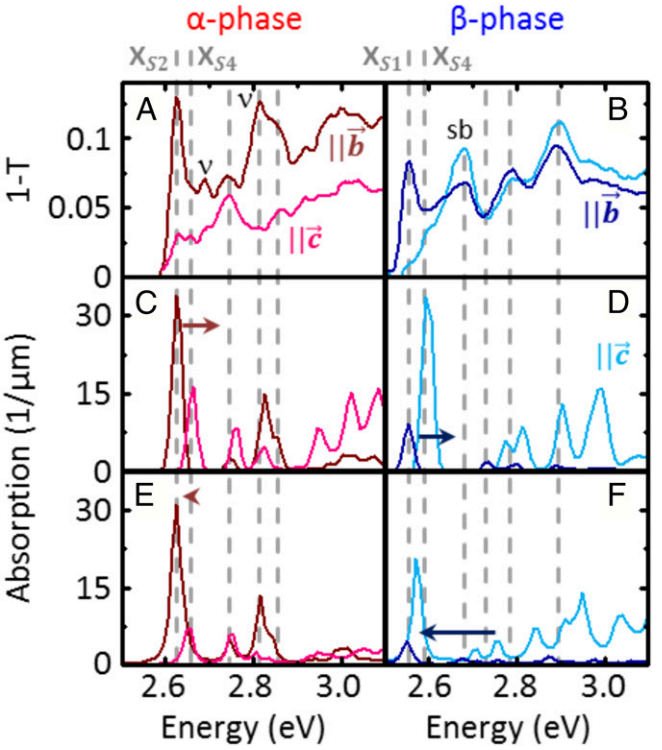

Fig. 2. Experimental (1-T) and calculated absorption spectra: Data for the α-phase are given in the *Left* column in red (*A*, *C*, and *E*) and β-phase results are shown in the *Right* column in blue (*B*, *D*, and *F*). Dark colors denote spectra polarized along the $\vec{b}$ axis; light colors show spectra polarized along the $\vec{c}$ axis. The first row (*A* and *B*) provides the experimental differential transmission spectra. The two peaks with the strongest vibronic contribution are marked by a ν. The second row (*C* and *D*) shows the calculated absorption beyond the TDA. The last row (*E* and *F*) provides the corresponding results using the TDA. The calculated spectra are shifted to match the optical gap of the experiment. Arrows on the lowest-lying lines symbolize the magnitude and direction of this shift. Gray dotted lines are drawn vertically through all subfigures of one species for facilitating the comparison of theory and experiment. The TDA does not lead to significant errors for the peak positions in the α-phase, but deviations from the full calculation are more clearly observed for the β-phase. We find theory and experiment to be in good agreement, with vibronic progressions accounting for all but one feature not present in the calculations and denoted by sb in *B*. The missing peak in the theory at 2.68 eV is assigned to a stopband.

characteristic for so-called J aggregates, including efficient emission and bathochromic behavior in the emission compared with the gas phase monomer (*Supporting Information*) (54). However, it is evident that electronic structure effects beyond dipole alignment are responsible for the significant differences between the absorption spectra of the two polymorphs, as we discuss below.

To understand the experimental optical data further, we analyze the results of the first-principles calculations. Computed optical absorption spectra are plotted in Fig. 2 *C* and *D*. Note that, in the comparison with experiment, we neglect the reflection contribution to the optical spectrum, which is constant within our theoretical framework and depends on the sample thickness. Overall, we find excellent agreement of the full BSE calculation with the experimental spectra after applying a small rigid shift (no larger than 50 meV, with magnitude and direction symbolized by arrows in Fig. 2) to our calculated spectra, so as to match the experimental onset. Such small shifts are well within the known accuracy of the ab initio GW-BSE approach (6, 36).

The calculated spectra show several excitations with nonvanishing oscillator strength, indicated by vertical dashed lines, with amplitudes resembling the calculated oscillator strength. The

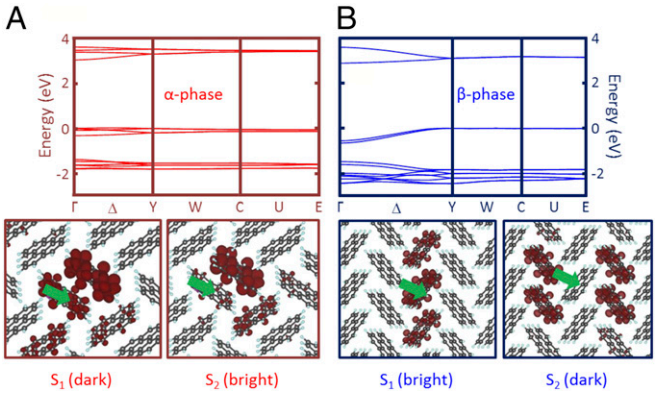

Fig. 3. Electronic band structure and excitonic wave functions: Calculated electronic band structure (*Top*) and exciton wave functions (*Bottom*) for the lowest-lying excitons in the α-phase (*A*) and the β-phase (*B*) of perylene. Lighter and darker colors denote results along the $\vec{c}$ axis and $\vec{b}$ axis, respectively. The red isosurfaces show the probability to find the electron given a hole fixed at the position of the green arrow. The two energetically degenerate lowest-lying excitons of each polymorph are shown.

transitions are broadened with a Gaussian of a 10-meV full-width half-maximum to reproduce the experimentally observed linewidth. Four nearly degenerate singlet states (X_{S1} to X_{S4}) are predicted for the energetically lowest-lying transitions for both polymorphs: X_{S1}, X_{S3}, and X_{S2}, X_{S3}, are dark states for the α- and β-phases, respectively, and hence are not visible in the absorption spectra. X_{S1} and X_{S2} are polarized perpendicular to X_{S3} and X_{S4}. The bright states are visible as two orthogonally polarized resonances in the linear absorption, in agreement with the phenomenological Davydov picture (53). The Davydov splitting is calculated to be 20 and 40 meV for the α- and β-phases, respectively. The first triplet excitation predicted by our calculations is at 1.7 eV. The energy of two triplets (3.4 eV) is considerably higher than the first singlet energy, ∼2.6 eV, thus ruling out singlet fission.

The high-precision experimental data given in Fig. 2 provide us with an opportunity to assess the accuracy of the TDA in predicting optical properties of aromatic compounds. Previously, the consequences of the TDA in the solid state has been explored in studies of optical properties of inorganic solids (55–57) and acene crystals (58), in some cases finding nonnegligible deviations with respect to full BSE calculations. The effect of the TDA for perylene is illustrated in Fig. 2 *E* and *F*. Reasonable agreement between experiment and our TDA calculations is found for both phases. The optical band gap obtained within the TDA overestimates experiment for the β-phase (by 71 meV along the $\vec{c}$ axis and 91 meV along the $\vec{b}$ axis), although the absolute position of the theoretical optical onset is difficult to obtain to a level of tens of millielectronvolts because of the inherent uncertainties in the GW approximation. This deviation is halved within the full-BSE calculations.

The major remaining discrepancy between theory and experiment is a spectrally broad, seemingly polarization-independent feature around 2.68 eV in the experimental β-phase transmission data (labeled "sb"). This feature is neither reproduced by theory nor assigned to vibronic replicas (51), as the latter would be strongly polarization dependent. We tentatively assign this feature to a polaritonic stopband (59, 60): a strong, characteristic reflection found between the transversal and the longitudinal exciton–polariton branches. Similar features are observed in quasi–one-dimensional polymer crystals and TCNQ crystals (61–64). They can be rationalized with the anticrossing rule for photons and an exciton resonance in the limit of strong coupling (65). The individual dispersion curves of both systems "avoid" each other, yielding a region in energy where light cannot propagate in the material and all light is reflected, ergo causing a "stopband" (sb).

To a first approximation, the width of the exciton–polariton stopband Δ_{LT} is related to the dimensionless oscillator strength f, the background dielectric index of the material ε_b, and the frequency of the exciton resonance ω_T by $\Delta_{LT} \approx f/\varepsilon_b\omega_T$. In the literature, the oscillator strength of the lowest-lying resonance in perylene is given as $f = 0.44$ (66). We estimate the background dielectric constant to be $\varepsilon_b = 1.7$ from our calculations (*Supporting Information*). To estimate Δ_{LT} for perylene, we compare it to a well-known material, in this case the organic molecular crystal 1,5-bis(dimethylamino)pentamethinium perchlorate (BDP) ($\hbar\omega_T = 3.1$ eV, $\varepsilon_b = 1.5$, $f = 3.31$, $\Delta_{LT} = 1.09$ eV) (67). Using the above numbers, we find the stopband width of perylene to be roughly 4% the size of Δ_{LT} as observed in BDP. Hence, we end up with an estimated stopband width for the lowest-lying exciton resonance for perylene of about 140 meV, which fits the observed spectra very well. Indeed, additional differential reflection measurements on β-phase perylene reveal the peak in question to be reflective in nature (see *Supporting Information* for details).

The stopband arises from forbidden propagation and thus is an effect of the refractive index (i.e., related to the real part of the dielectric function). This effect is commonly rather weak and will not be observed if the material is absorptive, that is, if we have significant contributions of the imaginary part of the dielectric function in the energy range above a transition. We hypothesize that the stopband is not seen in the α-phase because there is a dipole-allowed exciton that is close in energy.

Additional insight into the linear optical properties is gained by considering the calculated quasiparticle band structure, presented for the α- and β-phases in Fig. 3 *A* and *B*, respectively. For the α-phase, the calculated 3.0-eV direct fundamental gap between occupied and unoccupied molecular electronic bands at Γ is very close to the indirect one at 3.05 eV from the middle of the Γ–Y path to Γ. Mostly narrow bands are observed, as can be intuitively expected for weakly coupled van der Waals systems. For the β-phase, however, the calculated band structure shows significantly broader bands, with considerable dispersion found along the Δ direction (crystalline $\vec{b}$ axis in real space), where π-stacking is observed. The π-stacking leads to enhanced

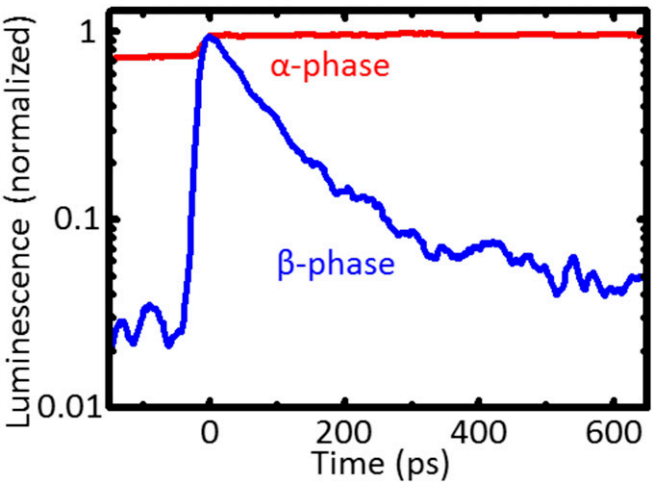

Fig. 4. Exciton lifetimes: Time-resolved photoluminescence measurements integrated over the primary excitonic emission channel for both phases, indicating that the β-phase shows faster photoluminescence decay than the α-phase despite comparable crystal quality. Data at negative times for the α-phase reflect the long exciton lifetimes, which exceed the inverse repetition rate of our exciting laser.

intermolecular interactions along this direction, which is expected to lead to broader dispersion in general (6, 29, 32, 33). The calculated 2.87-eV fundamental gap is indirect, from Y to Γ.

The *Bottom* panels of Fig. 3 *A* and *B* additionally illustrate the exciton wave functions associated with the two energetically degenerate lowest-energy exciton states of both polymorphs, where the amplitude for finding an electron is plotted for a fixed hole position (indicated by the green arrow). For the α-phase, the low-lying singlet states clearly reside mostly on one of the perylene dimers, with some smaller contributions found on neighboring dimers along the $\vec{b}$ axis. For the β-phase, there is significant delocalization in the relative electron–hole coordinate. Notably, the bright state displays delocalization exclusively along the $\vec{b}$ axis.

Consistent with previous studies (6, 29, 33), the extent and direction of exciton delocalization is strongly correlated with the extent and direction of band dispersion, which facilitates the delocalization. While exciton delocalization is not directly accessible in our experimental setup, we can test this prediction by probing exciton dynamics instead. The narrow energy spectrum of bands in the α-phase should translate into slow carrier relaxation dynamics. Conversely, significant band dispersion and exciton delocalization in the β-phase should result in much faster exciton decay. These expectations are confirmed by time-resolved photoluminescence spectroscopy experiments; the unpolarized time-resolved photoluminescence signals integrated around the fundamental exciton emission energies at 2.1 eV are depicted in Fig. 4. Indeed, the photoluminescence decay for the β-phase is significantly faster than for the α-phase. The latter displays an extremely long lifetime where a lower limit may be set to several tens of nanoseconds, whereas the former exhibits decay within a few hundreds of picoseconds.

In conclusion, we performed high-resolution measurements of the optical absorption for both polymorphs of high-quality single-crystal perylene samples, a model optoelectronic organic semiconductor. We obtain excellent agreement between experiment and many-body perturbation theory within the ab initio GW-BSE approach. This allows for a detailed analysis of the nature of the excitons and the relation between their wavefunction extent and band dispersion. It also facilitates an identification beyond-electronic effects, that is, vibronic replicas and evidence of an exciton–polariton stopband. We believe that these findings pose an important step toward the interpretation of more complex phenomena, such as dephasing and relaxation dynamics, as well as coupling to nonelectronic degrees of freedom.

Additional Information

Supporting Information contains further information on the polariton stopband identified in the crystalline absorption spectra, the calculated index of refraction of the crystal, the measured absorption spectra for gas- and crystal-phases, and the measured temperature-dependent absorption spectra.

ACKNOWLEDGMENTS. We acknowledge the use of computational resources at the National Energy Research Scientific Computing Center. Work at University of California, Berkeley, and Lawrence Berkeley National Laboratory was supported by the Center for Computational Study of Excited State Phenomena in Energy Materials at the Lawrence Berkeley National Laboratory, which is funded by the US Department of Energy, Office of Science, Basic Energy Sciences, Materials Sciences and Engineering Division, under Contract DE-AC02-05CH11231, as part of the Computational Materials Sciences Program. The Marburg group acknowledges financial support through the German Science Foundation (DFG) though Projects A2 (to G.W.) and B2 (to A.R.) of the Coordinated Research Center 1083, the Graduate College 1782 (to A.P.). Work at the Weizmann Institute is supported by the United States–Israel Binational Science Foundation. This work is also supported by the Molecular Foundry through the US Department of Energy, Office of Basic Energy Sciences, under the same contract number. The work at Giessen is partially supported through Projects CH660/2 and CH660/3 (to S.C.) of the DFG.

1. Brédas JL, Norton JE, Cornil J, Coropceanu V (2009) Molecular understanding of organic solar cells: The challenges. *Acc Chem Res* 42:1691–1699.
2. Crone B, et al. (2000) Large-scale complementary integrated circuits based on organic transistors. *Nature* 403:521–523.
3. Walker B, Port H, Wolf HC (1985) The two-step excimer formation in perylene crystals. *J Chem Phys* 92:177–185.
4. Toshiro S, et al. (1998) Excimer emission of anthracene, perylene, coronene and pyrene microcrystals dispersed in water. *Chem Phys Lett* 291:438–444.
5. Kolata K, Breuer T, Witte G, Chatterjee S (2014) Molecular packing determines singlet exciton fission in organic semiconductors. *ACS Nano* 8:7377–7383.
6. Kronik L, Neaton JB (2016) Excited-state properties of molecular solids from first principles. *Annu Rev Phys Chem* 67:587–616.
7. Smith MB, Michl J (2013) Recent advances in singlet fission. *Annu Rev Phys Chem* 64: 361–386.
8. Zhang X, et al. (2013) A potential perylene diimide dimer-based acceptor material for highly efficient solution-processed non-fullerene organic solar cells with 4.03% efficiency. *Adv Mater* 25:5791–5797.
9. Lin Y, et al. (2014) A star-shaped perylene diimide electron acceptor for high-performance organic solar cells. *Adv Mater* 26:5137–5142.
10. Alonso MI, Garriga M, Karl N, Ossó JO, Schreiber F (2002) Anisotropic optical properties of single crystalline PTCDA studied by spectroscopic ellipsometry. *Org Electron* 3:23–31.
11. Bulovic V, Burrows PE, Forrest SR, Cronin JA, Thompson ME (1996) Study of localized and extended excitons in 3, 4, 9, 10-perylenetetracarboxylic dianhydride (PTCDA). I. Spectroscopic properties of thin films and solutions. *Chem Phys* 210:1–12.
12. Hennessy MH, Soos ZG, Pascal RA, Girlando A (1999) Vibronic structure of PTCDA stacks: The exciton-phonon-charge-transfer dimer. *Chem Phys* 245:199–212.
13. Wewer W, Stienkemeier F (2003) Molecular versus excitonic transitions in PTCDA dimers and oligomers studied by helium nanodroplet isolation spectroscopy. *Phys Rev B* 67:125201.
14. Gisslén L, Scholz R (2009) Crystallochromy of perylene pigment: Interference between Frenkel excitons and charge-transfer states. *Phys Rev B* 80:115309.
15. Fuke K, Kaya K, Kaijiwara T, Nagakura S (1976) The polarized reflection and absorption spectra of perylene crystals in monomeric and dimeric forms. *J Mol Spectrosc* 63:98–107.
16. Forker R, Gruenewald M, Fritz T (2012) Optical differential reflectance spectroscopy on thin molecular films. *Annu Rep Prog Chem Sect C Phys Chem* 108:34–68.
17. Philpott MR (1980) Optical reflection spectroscopy of organic solids. *Annu Rev Phys Chem* 31:97–129.
18. Kamura Y, Shirotani I, Ohno K, Seki K, Inokuchi H (1976) Electronic spectra of perylene and coronene evaporated films as a function of their crystallinity. *Bull Chem Soc Jpn* 49:418–422.
19. Pick A, et al. (2015) Polymorph-selective preparation and structural characterization of perylene single crystals. *Cryst Growth Des* 15:5495–5504.
20. Tiago ML, Northrup JE, Louie SG (2003) Ab initio calculation of the electronic and optical properties of solid pentacene. *Phys Rev B* 67:115212.
21. Sharifzadeh S, Biller A, Kronik L, Neaton JB (2012) Quasiparticle and optical spectroscopy of the organic semiconductors pentacene and PTCDA from first principles. *Phys Rev B* 85:125307.
22. Rangel T, et al. (2016) Structural and excited-state properties of oligoacene crystals from first principles. *Phys Rev B* 93:115206.
23. Sharifzadeh S, Darancet P, Kronik L, Neaton JB (2013) Low-energy charge-transfer excitons in organic solids from first-principles: The case of pentacene. *J Phys Chem Lett* 4:2197–2201.
24. Refaely-Abramson S, et al. (2013) Gap renormalization of molecular crystals from density-functional theory. *Phys Rev B* 88:081204.
25. Refaely-Abramson S, et al. (2015) Solid-state optical absorption from optimally tuned time-dependent range-separated hybrid density functional theory. *Phys Rev B* 92:081204.
26. Hummer K, Puschnig P, Ambrosch-Draxl C (2004) Lowest optical excitations in molecular crystals: Bound excitons versus free electron-hole pairs in anthracene. *Phys Rev Lett* 92:147402.
27. Hummer K, Ambrosch-Draxl C (2005) Oligoacene exciton binding energies: Their dependence on molecular size. *Phys Rev B* 71:081202.
28. Hummer K, Puschnig P, Sagmeister S, Ambrosch-Draxl C (2006) Ab-initio study on the exciton binding energies in organic semiconductors. *Mod Phys Lett B* 20:261–280.
29. Ambrosch-Draxl C, et al. (2009) The role of polymorphism in organic thin films: Oligoacenes investigated from first principles. *New J Phys* 11:125010.
30. Cudazzo P, Gatti M, Rubio A (2012) Excitons in molecular crystals from first-principles many-body perturbation theory: Picene versus pentacene. *Phys Rev B* 86:195307.
31. Cudazzo P, Sottile F, Rubio A, Gatti M (2015) Exciton dispersion in molecular solids. *J Phys Condens Matter* 27:113204.
32. Yanagisawa S, Hamada I (2017) Determination of geometric and electronic structures of organic crystals from first principles: Role of the molecular configuration on the electronic structure. *J Appl Phys* 121:045501.
33. Sharifzadeh S, et al. (2015) Relating the physical structure and optoelectronic function of crystalline TIPS-pentacene. *Adv Funct Mater* 25:2038–2046.
34. Hybertsen MS, Louie SG (1985) First-principles theory of quasiparticles: Calculation of band gaps in semiconductors and insulators. *Phys Rev Lett* 55:1418–1421.
35. Hedin L (1965) New method for calculating the one-particle Green's function with application to the electron-gas problem. *Phys Rev* 139:A796.
36. Hybertsen MS, Louie SG (1986) Electron correlation in semiconductors and insulators: Band gaps and quasiparticle energies. *Phys Rev B Condens Matter* 34:5390–5413.

37. Rohlfing M, Louie SG (2000) Electron-hole excitations and optical spectra from first principles. *Phys Rev B* 62:4927–4944.
38. Onida G, Reining L, Rubio A (2002) Electronic excitations: Density-funcional versus many-body Green's function approaches. *Rev Mod Phys* 74:601–659.
39. Chai S, Wen S-H, Han K-L (2011) Understanding electron-withdrawing substituent effect on structural, electronic and charge transport properties of perylene bisimide derivatives. *Org Electron* 12:1806–1814.
40. Fedorov IA, Zhuravlev YN, Berveno VP (2013) Structural and electronic properties of perylene from first principles calculations. *J Chem Phys* 138:094509.
41. Shao M, Jornada FH, Yang C, Deslippe J, Louie SG (2016) Structure preserving parallel algorithms for solving the Bethe–Salpeter eigenvalue problem. *Linear Algebra Appl* 488:148–167.
42. Gonze X, et al. (2016) Recent developments in the ABINIT software package. *Comput Phys Commun* 205:106–131.
43. Botoshansky M, Herbstein FH, Kapon M (2003) Towards a complete description of polymorphic crystal: The example of perylene. *Helv Chim Acta* 86:1113–1128.
44. Perdew JP, Burke K, Ernzerhof M (1996) Generalized gradient approximation made simple. *Phys Rev Lett* 77:3865–3868.
45. Deslippe J, et al. (2012) BerkeleyGW: A massively parallel computer package for the calculation of the quasiparticle and optical properties of materials and nanostructures. *Comput Phys Commun* 183:1269–1289.
46. Joblin C, Salama F, Allamandola L (1999) Absorption and emission spectroscopy of perylene ($C_{20}H_{12}$) isolated in Ne, Ar, and N_2 matrices. *J Chem Phys* 115:7287–7297.
47. Cyvin SJ, Cyvin BN, Klaeboe P (1976) Condensed aromatics. Part XIX perylene. *Spectrosc Lett* 16:98.
48. Tan X, Salama F (2005) Cavity ring-down spectroscopy and theoretical calculations of the S1(1B3u)←S0(1Ag) transition of jet-cooled perylene. *J Chem Phys* 122:84318.
49. Halasinski TM, et al. (2003) Electronic absorption spectra of neutral perylene ($C_{20}H_{12}$), terrylene ($C_{30}H_{16}$), and quaterrylene ($C_{40}H_{20}$) and their positive and negative ions: Ne matrix-isolation spectroscopy and time-dependent density functional theory calculations. *J Phys Chem A* 107:3660–3669.
50. Donaldson D, Robertson J, White J (1953) The crystal and molecular structure of perylene. *Proc R Soc Lond A Math Phys Sci* 220:311–321.
51. Kosic TJ, Schosser CL, Dlott DD (1983) Vibrational spectroscopy of solid state molecular dimers. *Chem Phys Lett* 96:57–64.
52. Hestand NJ, Spano FC (2017) Molecular aggregate photophysics beyond the Kasha model: Novel design principles for organic materials. *Acc Chem Res* 50:341–350.
53. Kasha M (1963) Energy transfer mechanisms and the molecular exciton model for molecular aggregates. *Radiat Res* 20:55–70.
54. Hestand NJ, Spano FC (2015) Interference between coulombic and CT-mediated couplings in molecular aggregates: H- to J-aggregate transformation in perylene-based π-stacks. *J Chem Phys* 143:244707.
55. Olevano V, Reining L (2001) Excitonic effects on the silicon plasmon resonance. *Phys Rev Lett* 86:5962–5965.
56. Grüning M, Marini A, Gonze X (2009) Exciton-plasmon states in nanoscale materials: Breakdown of the Tamm-Dancoff approximation. *Nano Lett* 9:2820–2824.
57. Rocca D, Vörös M, Gali A, Galli G (2014) Ab initio optoelectronic properties of silicon nanoparticles: Excitation energies, sum rules, and Tamm-Dancoff approximation. *J Chem Theory Comput* 10:3290–3298.
58. Pusching P, Meisenbichler C, Draxl C (2013) Excited state properties of organic semiconductors; breakdown of the Tamm-Dancoff approximation. arXiv:1306.3790.
59. Fröhlich D, et al. (1990) Magnetic field splitting and dispersion of the lower 1S-excition polariton in Kl and Rbl. *Phys Status Solidi* 158:267–276.
60. Klingshirn CF (2005) *Semiconductor Optics* (Springer, Berlin).
61. Fincher CR, Jr, et al. (1979) Electronic structure of polyacetylene: Optical and infrared studies of undoped semiconducting $(CH)_x$ and heavily doped metallic $(CH)_x$. *Phys Rev B* 20:1589–1602.
62. Watanabe A, Tanaka M, Tanaka J (1981) Electrical and optical properties of a stable synthetic metallic polymer: Polypyrrole. *Chem Soc J* 54:2278–2281.
63. Pennelly RR, Eckhardt CJ (1976) Quasi-metallic reflection spectra of TCNQ single crystals. *Chem Phys* 12:89–105.
64. Wudl F (1984) From organic metals to superconductors: Managing conduction electrons in organic solids. *Acc Chem Res* 17:227–232.
65. Mills DL, Burstein E (1974) Polaritons: The electromagnetic modes of media. *Rep Prog Phys* 37:817–926.
66. Hochstrasser RM (1964) Spectral effects of strong exciton coupling in the lowest electronic transition of perylene. *J Chem Phys* 40:2559–2564.
67. Philpott MR (1970) Theory of molecular polaritons. Application of the reflection spectra of anthracene, 1,5-bis(dimethylamino)pentamethinium perchlorate, and some other cationic dye crystal. *J Chem Phys* 54:2120–2129.